Rif1 maintains telomeres and mediates DNA repair by encasing DNA ends

Article (Accepted Version)

Rif1 maintains telomeres and mediates DNA repair by encasing DNA ends

Stefano Mattarocci[1†], Julia K. Reinert[2,3†], Richard D. Bunker[2†], Gabriele A. Fontana[2†], Tianlai Shi[2,3,4], Dominique Klein[2], Simone Cavadini[2], Mahamadou Faty[2], Maksym Shyian[1], Lukas Hafner[1], David Shore[1*], Nicolas H. Thomä[2*], and Ulrich Rass[2*]

[1]Department of Molecular Biology and Institute of Genetics and Genomics in Geneva (iGE3), University of Geneva, Geneva, Switzerland.

[2]Friedrich Miescher Institute for Biomedical Research, Basel, Switzerland.

[3]Faculty of Natural Sciences, University of Basel, Basel, Switzerland.

[4]present address: Roche Innovation Center Basel, F. Hoffmann-La Roche Ltd, Basel, Switzerland

[†]These authors contributed equally to this work.

[*] to whom correspondence should be addressed:

David.Shore@unige.ch, Nicolas.Thoma@fmi.ch, Ulrich.Rass@fmi.ch

Abstract

In yeast, Rif1 is part of the telosome, where it inhibits telomerase and checkpoint signaling at chromosome ends. In mammalian cells, Rif1 is not telomeric but suppresses DNA end-resection at chromosomal breaks, promoting repair by non-homologous end-joining (NHEJ). Here, we describe crystal structures for the uncharacterized and conserved ~125 kDa N-terminal domain of Rif1 from *Saccharomyces cerevisiae* (Rif1-NTD), revealing an α-helical fold shaped like a shepherd's crook. We identify a high-affinity DNA-binding site in the Rif1-NTD, which fully encases DNA as a head-to-tail dimer. Engagement of the Rif1-NTD with telomeres proved essential for checkpoint control and telomere length regulation. Unexpectedly, Rif1-NTD also promoted NHEJ at DNA breaks in yeast, revealing a conserved role of Rif1 in DNA repair. We propose that tight associations between the Rif1-NTD and DNA gate access of processing factors to DNA ends, enabling Rif1 to mediate diverse telomere maintenance and DNA repair functions.

Introduction

Across organisms Rif1 participates in a multitude of seemingly unrelated genome maintenance processes ranging from DNA replication to DNA repair and telomere integrity[1]. During G1, Rif1 targets protein phosphatase 1 (PP1) to replication origins, thereby controlling the timing of origin firing, a role shared between yeast and mammalian cells[2-9]. In contrast, Rif1 functions in repair and telomere maintenance differ between organisms.

In yeast, but not in mammals, Rif1 is integral to the proteinaceous telosome structure that protects chromosome ends. Telomeres in budding yeast are organized around Rap1, which binds directly to double-stranded DNA (dsDNA) TG_{1-3} repeat sequences[10]. Rap1, through protein-protein interactions, recruits Rif1 and another protein, Rif2[11,12]. Together they form a protein meshwork that gives rise to a functional telomeric architecture[13]. Originally identified through a prominent role in telomere length regulation[11], Rif1 has the ability to inhibit the recruitment of telomerase and is involved in silencing the DNA damage checkpoint at telomeres[14-17]. The molecular processes underlying these activities remain unclear.

In mammalian cells, Rif1 modulates pathway choice in DNA double-strand break (DSB) repair, promoting NHEJ over homologous recombination (HR)-mediated repair. Mammalian Rif1 co-localizes with 53BP1 at DSBs[18-22], where its presence antagonizes DNA end-resection through an undefined mechanism. Rif1 thus stabilizes DNA ends and favors the repair of breaks through simple re-ligation[23-26]. There is currently no evidence for an analogous function of yeast Rif1 in DSB repair pathway choice, although Rif1 has been detected at DSBs in yeast[27,28].

Rif1 orthologs are highly divergent at the primary sequence level, but share a predicted N-terminal helical domain[29] of unknown function. Using budding yeast Rif1 as a model system, we identify the Rif1-NTD as a general modulator of DNA end-processing. Our structural and biochemical characterization demonstrates how Rif1-NTD restricts access of end-processing factors to DNA, providing Rif1 with a means to control diverse biological functions at telomeres as well as DSBs.

Results

Rif1-NTD forms an elongated, crook-shaped structural domain

All Rif1 orthologs contain a largely uncharacterized domain containing helical repeat elements[18,29]. In *S. cerevisiae* Rif1, this domain is predicted to reside within the first 1400 residues of its 1916 amino acids (Fig. 1a). An RVxF/SILK PP1 (Glc7 in yeast) binding motif (residues 116-118 and 147-149), which is found at varying positions in different Rif1 orthologs, precedes this putative domain and is essential for the replication timing function of Rif1[2-9,29]. The remaining C-terminal ~600 residues, which are largely unstructured, are specific to the budding yeast protein and contain the primary Rap1-binding motif (RBM; residues 1752-1772) with a major role in Rif1 telomere localization, and the Rif1 C-terminal domain (CTD; residues 1857-1916), a tetramerization module and low-affinity Rap1 binding site[13]. We identified the N-terminal domain comprising residues 177-1283 by limited proteolysis (data not shown; herein referred to as Rif1-NTD) and determined its crystal structure using a selenium multiple-wavelength anomalous dispersion approach. The model was built manually and refined at 3.95 Å resolution (Table 1). The Rif1-NTD assumes an extraordinarily elongated, crook-shaped fold spanning 238 Å (Fig. 1b). This domain, which is formed entirely by α-helices and connecting loops, contains a mixture of two-helix HEAT-like and three-helix armadillo-like modules. Rif1-NTD has three distinct regions: *i*) a curved N-terminal region (the 'HOOK': helical units 1-12, residues 185-874), (*ii*) a straight C-terminal portion (the 'SHAFT': units 16-23, residues 976-1272), and (*iii*) a boundary region marked by a kink followed by eight helices ('Transition': units 13-16, residues 875-975) oriented perpendicular to the other major helices in the domain. The HOOK is decorated by two insertion loops: Loop-I (residues 469-498), emerging from its convex face, and Loop-II (residues 676-715), emerging from its concave face. The HOOK contains the most conserved region (designated Rif1_N (PF12231) in Pfam[30]) (Supplementary Fig. 1a, 1b), comprising a sequence signature present in all Rif1 orthologs.

Rif1-NTD contains a DNA-binding site

Rif1-NTD co-purified with nucleic acids from insect cells, prompting us to explore a DNA-binding role. Following extensive screening with single-stranded (ss) DNA, dsDNA, and ssDNA/dsDNA junction substrates, crystals were obtained by mixing a Rif1 construct spanning amino acids 100-1322 with a 30 bp dsDNA carrying a 24 nt or 30 nt 3′ ssDNA tail (Rif1-NTD–DNA-1 and -2; Table 1). The crystals contained two conformationally distinct Rif1-NTD protomers in a figure-8-

shaped head-to-tail dimer arrangement, with DNA threaded through the two internal channels (designated DNA-binding channel I and II in Fig. 1c – e). Unequivocal electron density was found for linear dsDNA after refinement with an optimized bulk solvent model to ~6.5 Å resolution, enabling the entire 30 bp dsDNA portion of the crystallized construct to be modeled (Fig. 1d). No interpretable density was found for the ssDNA portion of the substrate, which is likely disordered (Supplementary Fig. 1c and Methods). Seeking independent evidence for functionally relevant Rif1-NTD–DNA configurations, we used negative stain electron microscopy (EM) (Supplementary Fig. 2a – h). Two-dimensional class averages and three-dimensional reconstructions confirmed the crook-shaped appearance of monomeric Rif1-NTD (Supplementary Fig. 2a, d), and established that it predominantly forms a figure-8-shaped head-to-tail dimer in the presence of DNA (ssDNA/dsDNA junction substrate) (Supplementary Fig. 2b, e), indicating that DNA binding in solution closely reflects the arrangement seen in the Rif1-NTD co-crystals with DNA (Fig. 1c).

The figure-8-shaped Rif1-NTD dimer bound DNA through DNA-binding channels I and II, each of which captures one of two distinct DNA molecules in the crystal. Each of the DNA molecules threads through channel I of one Rif1-NTD dimer and into channel II of a neighboring dimer, bridging adjacent Rif1-NTD dimers (Fig. 1d, e). Conformational differences between the Rif1-NTD dimer mates influence the architecture of the internal channels, which differ and vary from 34 to 42 Å in diameter (Supplementary Fig. 1d). Combined with the periodicity of the DNA and the offset of the two Rif1-NTD dimers bound to the same DNA (Supplementary Fig. 1e), this leads to variable DNA-binding in channel I and II in the crystal. Regardless of this apparent flexibility in DNA binding, dsDNA in each channel is surrounded by Rif1 with a 16 bp footprint.

Biochemical validation of high-affinity Rif1-NTD–DNA interactions

Rif1-NTD (construct spanning residues 100-1322) avidly bound the 3′-tailed ssDNA/dsDNA junction (30 bp + 30 nt tail) it crystallized with in vitro (Fig. 2a, b). Electromobility shift assays (EMSAs) showed up to four distinct retarded DNA species, consistent with multiple, oligomeric protein-DNA interactions as predicted by the structure. Quantification yielded an apparent K_d of ~20 nM for Rif1-NTD and the 3′-tailed ssDNA/dsDNA junction substrate. DNA binding as a function of protein concentration was non-hyperbolic and best fitted to the Hill equation assuming cooperative binding of Rif1-NTD to DNA (Methods). Rif1-NTD binding was also observed for duplex and ssDNA substrates (Supplementary Fig. 2i) with 3′-tailed ssDNA/dsDNA junctions exhibiting the strongest association with Rif1 (Supplementary Fig. 2j, k). Rif1 bound

DNA independently of the presence or absence of yeast telomeric TG_{1-3} repeats (Supplementary Fig. 2l).

The Rif1-NTD–DNA co-crystal structure shows that the DNA is wedged into the concave face of the HOOK by Loop-II emerging from helical unit 9, identifying these regions as predominant protein-DNA interaction sites (Fig. 2c). Here, we identified clusters of positively charged amino acids as potential protein-DNA contacts found within 8 Å of the DNA bound in channel I or II of the Rif1-NTD dimer (Supplementary Fig. 1f). In contrast, the less conserved (Supplementary Fig. 1a) and more flexible SHAFT element, which closes like a lid over the DNA buried inside the HOOK of the dimer mate (Fig. 1c), places different residues proximal to the DNA in channels I and II across crystals (Supplementary Fig. 1d). This makes it difficult to pinpoint key residues in the SHAFT that might mediate DNA interactions at the current resolution, and the SHAFT was omitted from further analysis.

On the concave face of the HOOK, the DNA is bound closest to helical units 4-8, which are part of the Rif1_N signature region defined by Pfam (helical units 1-8, Supplementary Fig. 1b). Twelve positively charged residues in helical units 4-8 are strategically positioned as potential DNA backbone contacts (R401, K406, K437, K451, K452, H561, K514, K518, K563, R565, K570, and R573; Supplementary Fig. 2m). These were targeted, and among several mutant versions of Rif1, a protein with amino acid substitutions K437E, K563E, and K570E (designated $Rif1_{HOOK}$; Fig. 2c, d) could be stably expressed in recombinant form for biochemical investigation (Supplementary Fig. 2n). Loop-II (residues 677-714, hereafter termed LOOP) bears a cluster of six positively charged residues (K680, R688, K689, K691, K692, K706, and K708), and we mutated two DNA-facing lysine residues (K691E and K692E) to generate a mutant designated $Rif1_{LOOP}$ (Fig. 2c and Supplementary Fig. 2n). Compared to wild-type Rif1-NTD, ~4-8-fold higher protein concentrations of $Rif1_{HOOK}$ and $Rif1_{LOOP}$ were needed to fully retard the labeled DNA in EMSAs (Fig. 2e). $Rif1_{HOOK}$ and $Rif1_{LOOP}$ therefore have compromised DNA-binding activity, showing that the regions within Rif1-NTD involved in duplex DNA interactions in the crystal are also involved in DNA binding in solution. We note that we have not been able to express stable constructs of Rif1 containing a minimal DNA binding domain consisting of only the HOOK domain, eliminating potential Rif1 dimerization surfaces. Rif1 dimerizes on DNA (Supplementary Fig. 2b, e), but we could hence not assess whether dimerization is strictly required for DNA binding.

Rif1-NTD is required for telomere length regulation

To assess the in vivo functions of the Rif1-NTD and its capacity to bind DNA, we first addressed its potential involvement in telomere length control, the canonical role of Rif1 in yeast. Consistent with previous results[13], Rif1 occupancy at native telomeres, measured by chromatin immunoprecipitation (ChIP), was reduced by 97% compared to wild-type Rif1 when the major Rap1 binding site was disrupted ($Rif1_{RBM}$ mutant I1762R, I1764R) (Fig. 3a, Supplementary Fig. 3a for protein expression). The $Rif1_{HOOK}$ DNA-binding mutant reduced the ChIP signal more moderately (~30%; Fig. 3a). The $Rif1_{HOOK/RBM}$ double mutant further diminished the residual telomere occupancy of $Rif1_{RBM}$, indicating that the $Rif1_{HOOK}$ and $Rif1_{RBM}$ together anchor Rif1 at telomeres (Supplementary Fig. 3b). Unexpectedly though, cells harboring the *rif1*$_{HOOK}$ allele exhibited a more severe telomere elongation phenotype (gain in length ~250 bp, phenocopying *rif1*Δ cells) than *rif1*$_{RBM}$ mutant cells (gain in length of ~150 bp) (Fig. 3b and Supplementary Fig. 3c). Cells expressing $Rif1_{LOOP}$ showed an intermediate telomere elongation phenotype, suggesting that $Rif1_{HOOK}$ is the more severely compromised Rif1-NTD mutant in vivo (Supplementary Fig. 3c). Thus, while the Rif1 RBM represents the major means of Rif1 recruitment to telomeres, the DNA-binding HOOK region and its ability to properly engage DNA is essential for mediating telomerase inhibition.

Rif1-NTD mediates the telomeric anti-checkpoint function of Rif1

In addition to inhibiting telomerase at normal-sized telomeres, Rif1 serves an anti-checkpoint function at eroded telomeres. This is evident in a model for critically short telomeres at HO endonuclease-induced DSBs flanked by short (80 bp) telomere repeat tracts (TG80), where Rif1 attenuates a transient DNA damage checkpoint response[15]. We determined cell-cycle restart times following induction of the HO endonuclease and found significant anti-checkpoint defects for cells harboring the *rif1*$_{HOOK}$ or *rif1*$_{LOOP}$ mutant alleles (Fig. 3C). In contrast, *rif1*$_{RBM}$ mutant cells behaved like *RIF1* wild-type cells, whereas *rif1*$_{HOOK/RBM}$ double mutant cells displayed a G2/M cell-cycle delay greater than that of either of the single mutants, approaching a *rif1*Δ phenotype (Fig. 3c). Checkpoint activation at TG80-flanked DSBs in the absence of Rif1 involves 5′ end-resection, generating 3′-terminated ssDNA bound by RPA[15], which provides the signal for activation of the apical ATR (Mec1) checkpoint kinase. We observed an increase in both ssDNA (Fig. 3d) and RPA binding (Fig. 3e) at TG80 ends after HO cut induction in the *rif1*$_{HOOK}$ mutant compared to wild-type or the *rif1*$_{RBM}$ mutant, despite $Rif1_{RBM}$ and $Rif1_{HOOK}$ exhibiting a similar level of recruitment (Fig. 3f; Supplementary Fig. 3d – f). These findings are consistent with a Rif1 HOOK anti-checkpoint effector function.

We then used strains carrying *cdc13* temperature-sensitive (ts) mutations, which exhibit no overt telomere abnormalities at the permissive temperature, but show telomere uncapping and synthetic lethality following deletion of *RIF1*[31-33]. We found that the Rif1 HOOK, but not the Rif1 RBM, is required for viability in *cdc13-ts* strains (Supplementary Fig. 4a, b), and that Rif1 attenuates resection of chromosome ends and RPA binding upon depletion from the nucleus[34] (Supplementary Fig. 4c – g). Thus, different models of critically short and uncapped telomeres show that the Rif1 HOOK domain and its ability to directly engage with its DNA substrate is required to counteract DNA end-resection and silence the DNA damage checkpoint.

An evolutionary conserved role of Rif1 in DSB repair, mediated by the Rif1-NTD

A Rif1 HOOK-mediated mechanism of attenuating DNA end-resection at TG80-flanked DSBs and eroded telomeres, independent of Rap1-binding, suggested a possible role of Rif1 at DNA breaks outside telomeric settings, akin to the DNA repair role of mammalian Rif1. We used a reporter strain in which an HO endonuclease-induced DSB at the *MAT* locus can only be repaired by NHEJ (Fig. 4a), providing a cell survival-based readout for NHEJ efficiency[35-37]. Compared to *RIF1* wild-type cells, we observed a ~40% drop in cell survival for *rif1*Δ mutants as measured by colony outgrowth following 2 h or 4 h of transiently induced HO endonuclease expression (Fig. 4b). Following chronic HO endonuclease expression, which only allows survival through rare imprecise NHEJ events that alter the DNA sequence of the HO cut site[36], we also observed a significant decrease in viability for *rif1*Δ compared to *RIF1* wild-type cells (Supplementary Fig. 5a). As expected, survival under acute or chronic HO endonuclease expression conditions was fully dependent on the core NHEJ factor Ku70[38-40] (Fig. 4b, Supplementary Fig. 5a). These findings establish Rif1 as a modulator of DSB repair by promoting NHEJ in yeast.

In a structure-function analysis, we found that cells expressing a C-terminally truncated Rif1 missing the Rap1 interaction motifs (RBM and CTD) did not exhibit a NHEJ phenotype (Supplementary Fig. 5b). The ability of Rif1 to modulate NHEJ thus resides in its N-terminal region, and is independent of Rap1. Expression of $Rif1_{RVxF/SILK}$ also gave no phenotype, demonstrating that recruitment of PP1/Glc7 to DSBs is not required for Rif1 to facilitate NHEJ repair (Fig. 4b). In contrast, cells expressing the $Rif1_{HOOK}$ DNA-binding mutant were as compromised in survival by NHEJ as *rif1*Δ cells (Fig. 4b). Consistent with a previous report[27], ChIP analyses showed that Rif1 accumulated at chromosome-internal DSBs (Fig. 4c, Supplementary Fig. 5c). Rif1 binding at chromosome-internal sites devoid of telomeric DNA sequences was independent of the RBM Rap1 interaction motif (Supplementary Fig. 5c, d).

Importantly, however, DSB binding required the Rif1 HOOK, and the NHEJ defect of the $Rif1_{HOOK}$ mutant correlated with ~50% reduction in Rif1 protein levels at DSBs at the *MAT* locus and elsewhere in the genome (Fig. 4c, Supplementary Fig. 5c). We conclude that the Rif1-NTD, and its DNA binding ability, is necessary and sufficient for the role of Rif1 in promoting NHEJ at induced DSBs.

We then examined the effect of Rif1 at stochastic breaks. Genetic disruption of NHEJ in yeast does not cause overt DNA damage sensitivity, but instead leads to a survival advantage in the presence of exogenous DSBs, consistent with HR being the preferred pathway for DSB repair under these conditions[41,42]. The contribution of NHEJ to break repair is evident in HR-deficient cells, where loss of NHEJ factors causes increased DNA damage sensitivity[38-40]. We found that deletion of *RIF1* increased cell survival upon chronic exposure to the radiomimetic drug Zeocin ~2-fold compared to wild-type cells. This effect was very similar to the phenotype caused by disruption of core end-joining factors such as *YKU70* (Fig. 4d), and was mediated by the Rif1 HOOK domain, but independent from PP1/Glc7 and Rap1 interactions (Supplementary Fig. 5e). In HR-deficient cells, which depend on NHEJ for DSB repair, loss of *RIF1* increased sensitivity to Zeocin (Supplementary Fig. 5f). These results demonstrate that the Rif1-NTD also functions in NHEJ at stochastic DNA breaks.

We found that loss of Rif1 or introduction of the HOOK mutation, resulted in a marked increase in ssDNA accumulation compared to *RIF1* wild-type at the HO endonuclease cleavage site near the *MAT* locus (Fig. 4a, e). Similar results were obtained at the *MNT2* locus (Supplementary Fig. 5g). Consistent with these findings, Southern blot analyses showed that the stability of a genomic fragment harboring the *MAT* locus after HO endonuclease cleavage was reduced in *rif1*Δ and $rif1_{HOOK}$ mutant cells compared to *RIF1* wild-type cells (Fig. 4f). Taken together, these findings show that Rif1 binds DSBs in vivo and attenuates DNA end-resection, facilitating re-ligation by the NHEJ pathway. The role of Rif1 in DSB repair pathway choice is thus conserved from yeast to human, and the Rif1-NTD DNA-binding domain is required for all functions of Rif1 involving telomeric and non-telomeric DNA ends.

Discussion

We identify the budding yeast Rif1-NTD as a high-affinity DNA-binding module that influences the processing of both chromosome breaks and telomeres. The structure of Rif1-NTD reveals a remarkably extended architecture (238 Å) that consists of an irregular α-helical repeat fold shaped like a shepherd's crook (Fig. 1b). In the presence of DNA, Rif1-NTD forms a figure-8-shaped head-to-tail dimer, encasing 16 bp segments of dsDNA (Fig. 1c – e, Supplementary Fig. 2a – h), primarily through interactions with its curved HOOK region. By successive loading of Rif1 molecules (Fig. 1d, e, 2a, b), arrays of yeast Rif1 would allow to form a protein sheath that, according to the structure, renders DNA inaccessible to other proteins.

In cells, we find that the Rif1-NTD promotes Rif1 accumulation at DNA ends, both as a standalone recruitment module, or supported by local interactions with Rap1 where telomeric DNA sequences are present (Fig. 3a, 4c, Supplementary Fig. 5c). In biochemical experiments the Rif1-NTD exhibits preference for 3′-tailed ssDNA/dsDNA junctions relative to simple ssDNA or dsDNA substrates of similar length (Supplementary Fig. 2j, k). As we find no evidence for telomere sequence-specific binding (Supplementary Fig. 2l), such structural preference for junction DNA provides a mechanism to guide Rif1 to its target sites at both telomeric ends and DNA breaks. Consistently, we find in vivo that Rif1 targets non-telomeric DSBs (Fig. 4c and Supplementary Fig. 5c), and show that yeast Rif1, like its mammalian counterpart, is involved in DSB repair pathway choice. This function strictly depends on the Rif1-NTD and its ability to properly engage DNA (Fig. 4b). At critically short telomeres, resected chromosome ends, and DSBs, the engagement of Rif1 with DNA attenuates DNA end-resection, which at DSBs imposes bias to NHEJ repair (Fig. 3d, e, 4e, f, Supplementary Fig. 4d – g, 5g).

Thus, Rif1-NTD acts as a recruitment module and as an effector module, which enables seemingly disparate Rif1 functions at DNA ends. Although Rif1 mutant proteins affected within the NTD HOOK region retain residual DNA binding in vitro (Fig. 2e) and in vivo (Fig. 3a, 3f, 4c, Supplementary Fig. 3e, 5c), their binding defects elicit severe and sometimes fully penetrant loss of function phenotypes in vivo (Fig. 3b, c, 4b, d, e, Supplementary Fig. 3c). This is most evident at telomeres, where the *rif1*$_{HOOK}$ allele conferred a more severe telomere length defect than the Rap1-binding defective *rif1*$_{RBM}$ allele, whereas the latter reduces Rif1 occupancy at telomeres more drastically (Fig. 3a, b). Our findings therefore support an end-effector function of the Rif1-NTD that goes beyond a mere recruitment role.

On the structural level, the Rif1-NTD DNA-binding mode is reminiscent of Ku70/80[43]. The Ku70/80 heterodimer encircles DNA within a ring-like channel, albeit using different structural motifs, binding with high-affinity and preventing access of other DNA repair factors. We propose an analogous model, where the diverse functions of Rif1 in telomere homeostasis, checkpoint control, and DSB repair are all mediated by directly blocking DNA end-processing factors (Fig. 5). Although DNA end-protection by Rif1 is ubiquitous, its ability to interact with Rap1 allows it to fulfill a specialized role at telomeres, which is unique to yeast. The biochemical properties of Rif1 described here help target Rif1 to diverse DNA ends, where its ability to cooperatively engage DNA enables protective binding along surrounding ssDNA and dsDNA regions. Our structural and functional studies in yeast thus reveal a unified mechanism underlying the diverse biological roles of Rif1 at telomeres and repair sites based on its ability to modulate access and processing of DNA ends.

Acknowledgements

We thank the following Technology Platform members of the Friedrich Miescher Institute: A. Graff-Meyer and A. Schenk (Electron Microscopy Facility) for assistance in the collection of the negative stain EM data and analysis; D. Hess (Proteomics and Protein Analysis) for support with protein analyses; H. Gut and J. Keusch (Protein Structure) for support with protein crystallization and crystallographic data collection. Crystallographic experiments were performed at beamline X06SA and X06DA of the Swiss Light Source, Paul Scherrer Institut, Switzerland. J.K.R. was supported by a Boehringer Ingelheim Fonds PhD fellowship, L.H. by an Excellence Master fellowship from the University of Geneva. Work in the laboratory of U.R. is supported by the Swiss Cancer League & Swiss Cancer Research, and the Novartis Research Foundation. The laboratory of N.H.T. is supported by the Novartis Research Foundation. This project received funding from the European Research Council (ERC) under the European Union's Horizon 2020 research and innovation programme (grant agreement No. 666068, N.H.T.). Work in the laboratory of D.S. and N.H.T was supported by the Swiss National Science Foundation (grant 31003A_149463 to D.S., and Sinergia grant CRSII3_160734 to D.S. and N.H.T.). We thank S. Gasser for providing yeast strains and reagents, and for fruitful discussions. We would like to thank all members of the Gasser, Thomä, Rass, and Shore laboratories for valuable input and technical assistance.

Author Contributions

U.R., N.H.T., and D.S., conceived this study. J.K.R and T.S. expressed and purified recombinant proteins helped by M.F and produced crystals helped by R.D.B. J.K.R., T.S. and R.D.B. collected crystallographic data. R.D.B. carried out the crystallographic analysis and interpreted the results. J.K.R. designed, performed and analyzed electromobility shift assays helped by D.K. J.K.R. designed and performed the negative stain EM experiments and analyzed the results helped by S.C. S.M. designed, performed and analyzed Western Blot and ChIP experiments helped by M.S. and L.H. S.M. designed, performed and analyzed the assay to measure checkpoint activation, the assays to score the viability of ts mutants and the Southern blots to assess telomere length. S.M. and G.A.F. performed and analyzed the qPCR experiments to measure ssDNA formed by DNA end-resection. G.A.F. designed and analyzed the colony outgrowth assays to score NHEJ efficiency and DNA damage resistance; data collection was performed with blinding by G.A.F. and D.K. G.A.F. designed, performed and analyzed DSB stability experiments by Southern blotting helped by D.K. S.M., J.K.R., R.D.B.

and G.A.F contributed equally to this work. All the authors discussed the data. U.R., N.H.T. and D.S. wrote the manuscript with input from S.M., J.K.R., R.D.B. and G.A.F.

Competing Financial Interest Statement

The authors declare no competing financial interest.

References

1. Mattarocci, S., Hafner, L., Lezaja, A., Shyian, M. & Shore, D. Rif1: A Conserved Regulator of DNA Replication and Repair Hijacked by Telomeres in Yeasts. *Front. Genet.* **7**, 45 (2016).

2. Mattarocci, S. et al. Rif1 controls DNA replication timing in yeast through the PP1 phosphatase Glc7. *Cell Rep.* **7**, 62-9 (2014).

3. Dave, A., Cooley, C., Garg, M. & Bianchi, A. Protein phosphatase 1 recruitment by Rif1 regulates DNA replication origin firing by counteracting DDK activity. *Cell Rep.* **7**, 53-61 (2014).

4. Hiraga, S. et al. Rif1 controls DNA replication by directing Protein Phosphatase 1 to reverse Cdc7-mediated phosphorylation of the MCM complex. *Genes Dev.* **28**, 372-83 (2014).

5. Cornacchia, D. et al. Mouse Rif1 is a key regulator of the replication-timing programme in mammalian cells. *EMBO J.* **31**, 3678-90 (2012).

6. Hayano, M. et al. Rif1 is a global regulator of timing of replication origin firing in fission yeast. *Genes Dev.* **26**, 137-50 (2012).

7. Yamazaki, S., Hayano, M. & Masai, H. Replication timing regulation of eukaryotic replicons: Rif1 as a global regulator of replication timing. *Trends Genet.* **29**, 449-60 (2013).

8. Yamazaki, S. et al. Rif1 regulates the replication timing domains on the human genome. *EMBO J.* **31**, 3667-77 (2012).

9. Peace, J.M., Ter-Zakarian, A. & Aparicio, O.M. Rif1 regulates initiation timing of late replication origins throughout the S. cerevisiae genome. *PLoS One* **9**, e98501 (2014).

10. Konig, P., Giraldo, R., Chapman, L. & Rhodes, D. The crystal structure of the DNA-binding domain of yeast RAP1 in complex with telomeric DNA. *Cell* **85**, 125-36 (1996).

11. Hardy, C.F., Sussel, L. & Shore, D. A RAP1-interacting protein involved in transcriptional silencing and telomere length regulation. *Genes Dev.* **6**, 801-14 (1992).

12. Wotton, D. & Shore, D. A novel Rap1p-interacting factor, Rif2p, cooperates with Rif1p to regulate telomere length in Saccharomyces cerevisiae. *Genes Dev.* **11**, 748-60 (1997).

13. Shi, T. et al. Rif1 and Rif2 shape telomere function and architecture through multivalent Rap1 interactions. *Cell* **153**, 1340-53 (2013).

14. Bianchi, A. & Shore, D. Increased association of telomerase with short telomeres in yeast. *Genes Dev.* **21**, 1726-30 (2007).

15. Ribeyre, C. & Shore, D. Anticheckpoint pathways at telomeres in yeast. *Nat. Struct. Mol. Biol.* **19**, 307-13 (2012).

16. Sabourin, M., Tuzon, C.T. & Zakian, V.A. Telomerase and Tel1p preferentially associate with short telomeres in S. cerevisiae. *Mol. Cell* **27**, 550-61 (2007).

17. Hirano, Y., Fukunaga, K. & Sugimoto, K. Rif1 and rif2 inhibit localization of tel1 to DNA ends. *Mol. Cell* **33**, 312-22 (2009).

18. Silverman, J., Takai, H., Buonomo, S.B., Eisenhaber, F. & de Lange, T. Human Rif1, ortholog of a yeast telomeric protein, is regulated by ATM and 53BP1 and functions in the S-phase checkpoint. *Genes Dev.* **18**, 2108-19 (2004).

19. Xu, L. & Blackburn, E.H. Human Rif1 protein binds aberrant telomeres and aligns along anaphase midzone microtubules. *J. Cell Biol.* **167**, 819-30 (2004).

20. Buonomo, S.B.C., Wu, Y., Ferguson, D. & de Lange, T. Mammalian Rif1 contributes to replication stress survival and homology-directed repair. *J.Cell Biol* **187**, 385-398 (2009).

21. Fradet-Turcotte, A. et al. 53BP1 is a reader of the DNA-damage-induced H2A Lys 15 ubiquitin mark. *Nature* **499**, 50-4 (2013).

22. Wilson, M.D. et al. The structural basis of modified nucleosome recognition by 53BP1. *Nature* **536**, 100-3 (2016).

23. Escribano-Diaz, C. et al. A cell cycle-dependent regulatory circuit composed of 53BP1-RIF1 and BRCA1-CtIP controls DNA repair pathway choice. *Mol. Cell* **49**, 872-83 (2013).

24. Chapman, J.R. et al. RIF1 is essential for 53BP1-dependent nonhomologous end joining and suppression of DNA double-strand break resection. *Mol. Cell* **49**, 858-71 (2013).

25. Di Virgilio, M. et al. Rif1 prevents resection of DNA breaks and promotes immunoglobulin class switching. *Science* **339**, 711-5 (2013).

26. Zimmermann, M., Lottersberger, F., Buonomo, S.B., Sfeir, A. & de Lange, T. 53BP1 regulates DSB repair using Rif1 to control 5' end resection. *Science* **339**, 700-4 (2013).

27. Martina, M., Bonetti, D., Villa, M., Lucchini, G. & Longhese, M.P. Saccharomyces cerevisiae Rif1 cooperates with MRX-Sae2 in promoting DNA-end resection. *EMBO Rep.* **15**, 695-704 (2014).

28. Ira, G. & Nussenzweig, A. A new Riff: Rif1 eats its cake and has it too. *EMBO Rep.* **15**, 622-4 (2014).

29. Sreesankar, E., Senthilkumar, R., Bharathi, V., Mishra, R.K. & Mishra, K. Functional diversification of yeast telomere associated protein, Rif1, in higher eukaryotes. *BMC Genomics* **13**, 255 (2012).

30. Finn, R.D. et al. The Pfam protein families database: towards a more sustainable future. *Nucleic Acids Res.* **44**, D279-85 (2016).

31. Anbalagan, S., Bonetti, D., Lucchini, G. & Longhese, M.P. Rif1 supports the function of the CST complex in yeast telomere capping. *PLoS Genet.* **7**, e1002024 (2011).

32. Xue, Y., Rushton, M.D. & Maringele, L. A novel checkpoint and RPA inhibitory pathway regulated by Rif1. *PLoS Genet.* **7**, e1002417 (2011).

33. Zubko, M.K., Guillard, S. & Lydall, D. Exo1 and Rad24 differentially regulate generation of ssDNA at telomeres of Saccharomyces cerevisiae cdc13-1 mutants. *Genetics* **168**, 103-15 (2004).

34. Haruki, H., Nishikawa, J. & Laemmli, U.K. The anchor-away technique: rapid, conditional establishment of yeast mutant phenotypes. *Mol. Cell* **31**, 925-32 (2008).

35. Lee, S.E., Paques, F., Sylvan, J. & Haber, J.E. Role of yeast SIR genes and mating type in directing DNA double-strand breaks to homologous and non-homologous repair paths. *Curr. Biol.* **9**, 767-70 (1999).

36. Moore, J.K. & Haber, J.E. Cell cycle and genetic requirements of two pathways of nonhomologous end-joining repair of double-strand breaks in Saccharomyces cerevisiae. *Mol. Cell Biol.* **16**, 2164-73 (1996).

37. Horigome, C. et al. PolySUMOylation by Siz2 and Mms21 triggers relocation of DNA breaks to nuclear pores through the Slx5/Slx8 STUbL. *Genes Dev.* **30**, 931-45 (2016).

38. Boulton, S.J. & Jackson, S.P. Identification of a Saccharomyces cerevisiae Ku80 homologue: roles in DNA double strand break rejoining and in telomeric maintenance. *Nucleic Acids Res.* **24**, 4639-48 (1996).

39. Mages, G.J., Feldmann, H.M. & Winnacker, E.L. Involvement of the Saccharomyces cerevisiae HDF1 gene in DNA double-strand break repair and recombination. *J. Biol. Chem.* **271**, 7910-5 (1996).

40. Siede, W., Friedl, A.A., Dianova, I., Eckardt-Schupp, F. & Friedberg, E.C. The Saccharomyces cerevisiae Ku autoantigen homologue affects radiosensitivity only in the absence of homologous recombination. *Genetics* **142**, 91-102 (1996).

41. Clikeman, J.A., Khalsa, G.J., Barton, S.L. & Nickoloff, J.A. Homologous recombinational repair of double-strand breaks in yeast is enhanced by MAT heterozygosity through yKU-dependent and -independent mechanisms. *Genetics* **157**, 579-89 (2001).

42. Zhang, Y. et al. Role of Dnl4-Lif1 in nonhomologous end-joining repair complex assembly and suppression of homologous recombination. *Nat. Struct. Mol. Biol.* **14**, 639-46 (2007).

43. Walker, J.R., Corpina, R.A. & Goldberg, J. Structure of the Ku heterodimer bound to DNA and its implications for double-strand break repair. *Nature* **412**, 607-14 (2001).

44. Zierhut, C. & Diffley, J.F. Break dosage, cell cycle stage and DNA replication influence DNA double strand break response. *EMBO J.* **27**, 1875-85 (2008).

45. Adams, P.D. et al. PHENIX: a comprehensive Python-based system for macromolecular structure solution. *Acta Cryst. D* **66**, 213-221 (2010).

46. Chen, V.B. et al. MolProbity: all-atom structure validation for macromolecular crystallography. *Acta Cryst. D* **66**, 12-21 (2010).

Figure legends

Figure 1: Crystal structures of Rif1-NTD in isolation and in complex with DNA. (**a**) Rif1 domain organization with the RVxF/SILK, Rap1 binding motif (RBM), C-terminal domain (CTD) (green) and Rif1-NTD (blue) functional regions. A sequence identity histogram from a structure-guided sequence alignment of 17 yeast Rif1 orthologs is shown above (details in Supplementary Fig. 1a). The expanded view shows the organization of the two- and three-helix units found in the crystal structure. The HOOK region (dark blue), SHAFT region (light blue), insertion loops I and II (mauve), and a transition region (gray) are indicated. (**b**) Rif1-NTD overall fold and (**c**) Rif1-NTD in complex with DNA in cartoon representation (see also Supplementary Fig. 1c to 1e). (**d**) Cross-section of the two Rif1-NTD dimers bound to each 30 bp dsDNA with an unbiased segment of its 2mF_o-DF_c electron density (gray mesh) contoured at 0.8 r.m.s.d and shown at a 4 Å radius around the DNA (see also Supplementary Fig. 1c and Methods). The Rif1-NTD surface within 8 Å of the DNA is shown in red. No interpretable electron density was found for the 30 nt ssDNA 3′-tail of the crystallized dsDNA. (**e**) View of c expanded by crystallographic symmetry showing how multiple Rif1-NTD dimers (blue surfaces) bind the same two DNA molecules in the Rif1-NTD co-crystals with DNA.

Figure 2. The Rif1-NTD HOOK domain binds DNA. (**a**) EMSA analysis using 1 nM of a ^{32}P labeled 3′-tailed 30 nt + 30 bp ssDNA/dsDNA junction substrate with increasing concentrations of Rif1-NTD (4-40 nM). (**b**) Rif1-NTD binds 3′-tailed DNA cooperatively with low nanomolar affinity. Band intensities were quantified relative to total signal in each lane and plotted. The resulting binding curve was best accounted by a Hill slope (see Online Methods). (**c**) Rif1-NTD surface electrostatic potential with close-up view of the Rif1 HOOK domain. (**d**) Schematic representation of Rif1-NTD (residues 100 to 1322) indicating the location of the $Rif1_{HOOK}$ (blue) and $Rif1_{LOOP}$ (green) mutations and their position in the Rif1 crystal structure relative to the DNA. (**e**) $Rif1_{HOOK}$ and $Rif1_{LOOP}$ mutants have lower binding affinity for dsDNA than wild-type Rif1. EMSA analysis using 1 nM ^{32}P-labeled 30 bp dsDNA with increasing concentrations (5, 10, 20 and 40 nM) of wild-type or mutant Rif1-NTD with quantification (individual values plotted and mean values presented as curves, n = 2, independent experiments). (**a**, **e**) Uncropped gel images are in the Supplementary Data Set.

Figure 3. Rif1-NTD is an effector of telomere homeostasis at native and critically short telomeres. (**a**) ChIP analysis of Myc-tagged wild-type Rif1, or the indicated mutants, at native telomeres VI-R (blue) and XV-L (red). Results are reported as average fold-enrichment relative to *ACT1* ± s.d. (n = 5). (**b**) Telomere length analyzed at telomeric Y' elements. Southern blots were performed with genomic DNA digested with *Xho*I using a radiolabeled TG_{1-3} repeat probe. Uncropped gel image is shown in the Supplementary Data Set. (**c**) Percentage of large-budded, G2/M-arrested cells following HO endonuclease induction in wild-type or *rif1* mutant cells presented as Kaplan-Meier survival analysis. Average G2/M to G1 transition times (t), number of cells examined for each sample (n) and P-values are indicated. (**d**) Percentage of ssDNA formed at three sites of increasing distance from a TG80-flanked DSB HO cut site, reported as mean values ± s.d. (n = 4). (**e**) ChIP analysis of RPA recruitment at a TG80-flanked DSB in the

indicated strains. Results for centromere-proximal (green) and telomere-proximal (blue) RPA accumulation are reported as average fold-enrichment relative to *ACT1* ± s.d. (*n* = 4). (**f**) ChIP analysis at either side of a TG80-flanked DSB of cells expressing Myc-tagged Rif1 wild-type and the indicated mutants before (0 h) and after (2 h) HO endonuclease induction, reported as average fold-enrichment relative to *ACT1* ± s.d. (*n* = 4). Experiments in panels (**a**) and (**d – f**) were performed as independent biological replicates.

Figure 4. Rif1-NTD attenuates end-resection at chromosome-internal DSBs to promote DNA repair by NHEJ. (**a**) Overview of *S. cerevisiae* chromosome III harboring the *MAT*α HO endonuclease cut site and deleted for the homologous donor loci (*hml*Δ/*hmr*Δ). HO endonuclease is induced by galactose addition and the resulting DSB can only be repaired by NHEJ. Primer pairs used for ChIP analyses of Rif1-Myc recruitment (blue) and qPCR to study DNA end-resection (red) are indicated. DNA end-resection progressively destroys the annotated *Alu*I restriction sites, leading to increased qPCR product yield, which serves as a measure for the level of ssDNA formation[44]. (**b**) NHEJ efficiency measured by colony outgrowth after acute HO endonuclease induction. Data are presented as mean values ± s.e.m. (*n* = 6). PE, plating efficiency, PE_{T0}, plating efficiency before HO endonuclease induction. (**c**) ChIP analysis of the recruitment of Myc-tagged wild-type and mutant versions of Rif1 at the *MAT*α HO endonuclease cut site. Results are reported as average fold-enrichment relative to the *ACT1* gene ± s.d. (*n* = 3). (**d**) Cell viability in the presence of 70 µg/mL Zeocin. Data are presented as mean values ± s.e.m. (*n* = 6). (**e)** ssDNA formed by DNA end-resection as measured by qPCR. Data are presented as mean values ± s.e.m. (*n* = 4). (**f**) Analysis of DSB ends destabilization by Southern blotting. *Top left*, Schematic representation of the *MAT*α locus. The location of the Southern probe, the *Eco*RV restriction sites used for DNA digestion, and the size of the detected bands are indicated[42]. *Bottom left*, percentage of remaining DNA relative to the 1 h time point. Data are presented as mean values ± s.e.m. (*n* = 4). *Right*, representative Southern blots. The *SMC2* locus (designated S) served as loading control and for normalization. Experiments in panels (**b – f**) were performed as independent biological replicates. Uncropped gel images are in the Supplementary Data Set.

Figure 5. Rif1-NTD controls the fate of DNA ends at telomeres and chromosome breaks. (**a**) At native *S. cerevisiae* telomeres, Rap1 recruits Rif1 and Rif2 to form an intricate protective protein sheath[13], while Cdc13-Stn1-Ten1 (CST) cover the ssDNA overhang. Telomerase inhibition is dependent on the newly identified Rif1-NTD DNA-binding activity, which may contribute to telomere architecture by engaging unoccupied dsDNA and ssDNA proximal to Rap1 sites. Note that while one dsDNA is shown bound per Rif1-NTD dimer, two DNA molecules could conceivably be bound by each Rif1-NTD dimer, as seen in the crystal structure. (**b**) The Rif1-NTD also engages DNA ends in a Rap1-independent manner, coating ssDNA/dsDNA junctions at chromosome-internal breaks. Rif1-NTD binding DNA at chromosome breaks blocks end-resection, stabilizes DNA ends and facilitates NHEJ. By binding cooperatively, Rif1 is equipped to spread into neighboring DNA regions, insulating the DNA and preventing access of processing factors, a mechanism shared between telomeres and chromosome breaks. Crystallographic models for Rif1-NTD, Rif1-CTD and RBM (blue)[13], Rap1

(light gray), Rif2 (green) and CST (gray) are shown as solid outlines. Dotted lines indicate unstructured parts of Rif1 and Rif2.

Table 1. Crystallographic data collection and refinement statistics.

	RIF1-NTD-1 (PDB code 5NVR)	RIF1-NTD–DNA-1	RIF1-NTD–DNA-2 (PDB code 5NW5)
Data collection[a]			
Wavelength (Å)	0.9790	1.0000	0.9186
Space group	$P6_522$	$P2_12_12_1$	$P2_12_12_1$
Unit cell (Å)	$a = b = 203.57$, $c = 197.723$	$a = 81.93$, $b = 157.60$, $c = 385.19$	$a = 92.16$, $b = 169.88$, $c = 390.26$
Resolution (Å)[b]	50–3.94 (4.16–3.94)	58.02–4.40 (4.64–4.40)	43.25–6.50 (7.27–6.50)
Unique reflections	21894 (3132)	32678 (4704)	12703 (3529)
Multiplicity	50.6 (42.7)	6.3 (5.8)	11.9 (12.5)
Completeness (%)	100 (100)	99.9 (100)	99.6 (100)
$\langle I/\sigma(I)\rangle$	14.4 (1.3)	5.5 (0.6)	8.0 (0.5)
$CC_{1/2}$ outer shell; no. of pairs	0.497; n =3129	0.172; n =4689	0.142; n = 3529
Resolution (Å) where			
$\langle I/\sigma(I)\rangle > 2.0$ (overall)	4.16	6.10	7.56
$\langle I/\sigma(I)\rangle > 2.0$ (along h)	-	6.11	7.83
$\langle I/\sigma(I)\rangle > 2.0$ (along k)	-	8.10	10.16
$\langle I/\sigma(I)\rangle > 2.0$ (along l)	-	5.25	7.11
$CC_{1/2} > 0.3$ (overall)	3.94	4.96	7.09
$CC_{1/2} > 0.3$ (along h)	-	4.76	7.19
$CC_{1/2} > 0.3$ (along k)	-	7.01	9.91
$CC_{1/2} > 0.3$ (along l)	-	5.25	6.50
R_{meas}	0.234 (4.131)	0.264 (3.294)	0.358 (6.001)
R_{pim}	0.033 (0.629)	0.114 (1.496)	0.101 (1.757)
Wilson B-factor (A^2)[c]	183	220	389
Refinement			
Resolution range (Å)	49.29–3.94 (4.09–3.94)	-	43.25–6.50 (7.15–6.50)
Reflections	21814 (2125)	-	8873 (732)
Reflections (R_{free})	1132 (115)	-	578 (59)
Completeness (%)	100 (100)	-	70.0 (23.9)
Complete to resolution (Å)	3.94	-	9.09
R_{work} / R_{free}	0.2115 / 0.2609	-	0.2529 / 0.2772
No. non-hydrogen atoms	8691	-	18864
Average B-factor ($Å^2$)		-	
Protein / DNA	221 / -	-	316 / 547
R.m.s bonds (Å) / angles (°)	0.003 / 0.54	-	0.015 / 2.12
Ramachandran plot (%)[d]			
Favored	91	-	85.8
Allowed	7.2	-	11.3
Outliers	1.6	-	2.9

[a]All data sets collected from single crystals
[b]Values in parenthesis are for the highest-resolution shell
[c]From *phenix.xtriage*[45]
[d]From *Molprobity*[46]

Online methods

Rif1-NTD protein purification

Saccharomyces cerevisiae Rif1 N-terminal domain (Rif1-NTD) constructs (residues 177-1283 or 100-1322) and mutants (residues 100-1322 of HOOK, K437E/K563E/K570E; LOOP, K691E/K692E) were expressed as N-terminal Strep(II)-tag fusions in *Trichoplusia ni* High Five insect cells (Life Technologies). Bacmids, primary and secondary viruses were produced using the Bac-to-Bac system (Life Technologies) and *Spodoptera frugiperda* (Sf9) insect cells (ThermoFisher Scientific). High Five insect cells were grown in SF900-II medium (Life technologies) at 27°C and infected at a cell density of 4 x 10^6 mL with 15 mL/L of P2 virus solution. Cells were harvested by centrifugation 48 h after infection and lysed by sonication in 50 mM Tris-HCl pH 8.0, 500 mM NaCl, 1 mM tris(2-carboxyethyl)phosphine (TCEP), 1 mM phenylmethylsulfonyl fluoride, 1 × protease inhibitor cocktail (Sigma), 5 mM β-mercaptoethanol. After clarification by ultracentrifugation (45,000*g* for 45 min at 4°C), the Rif1-NTD was extracted by Strep-Tactin affinity (Strep-Tactin Sepharose, IBA). The fusion tag was removed by overnight incubation with 5% (w/w) TEV protease. The protein solution was concentrated by ultrafiltration (30 kDa molecular-weight cutoff concentrator; Macrosep, Pall) and separated by size exclusion chromatography (Superdex 200, GE Healthcare) in 50 mM HEPES pH 7.4, 310 mM NaCl, 1 mM TCEP (storage buffer). Purified Rif1-NTD was concentrated by ultrafiltration to 60 µM, flash-frozen in liquid nitrogen and stored at -80°C.

Expression and purification of selenomethionine-labeled Rif1-NTD

Selenomethionine-substituted (SeMet) Rif1-NTD (residues 177-1283) was produced according to the procedure in Cronin et al.[47] except infected High Five cells were cultured in methionine and cysteine-free SF900–II medium supplemented with 2 mM L-glutamine, 2 mM L-cysteine, and 20 mg/L L-selenomethionine and 8 h post-infection a further 40 mg/L L-selenomethionine was added. SeMet Rif1-NTD (residues 177-1283) was purified in the same manner as the native protein.

Rif1-NTD structure determination

Crystals of Rif1-NTD (residues 177-1283) were grown by hanging-drop vapor diffusion at 22°C from drops prepared by mixing 1 µL of protein solution (3.8 mg/mL in storage buffer) with 1 µL of reservoir solution (100 mM Tris-HCl, pH 7.5, 320 mM lithium sulfate, 850 mM potassium sodium tartrate). SeMet-substituted crystals were grown in the same conditions from seeds prepared from native Rif1-NTD (residues 177-1283) crystals, which were transferred into pre-equilibrated drops (4-16 h) with a cat whisker. Crystals appeared within 4 d and were harvested after two weeks. Prior to X-ray analysis, each crystal was swept briefly through a cryoprotectant solution composed of reservoir solution supplemented with 20% (v/v) ethylene glycol then flash-cooled in liquid nitrogen.

A gold derivative was prepared by soaking a native crystal with 1 mM $KAu(CN)_2$ in a stabilizing solution formulated to reproduce the crystal-growth condition as closely as possible (artificial mother liquor). Crystals were immersed in 4 µL drop of soaking solution and incubated for 1.5 h at 20°C with hanging-drop vapor diffusion over a reservoir of stabilizing solution. The crystals were back-soaked for 5 min in a fresh 10 µL drop of stabilizing solution before proceeding to X-ray analysis as for other crystals.

Diffraction data were collected at the Swiss Light Source, Switzerland, from beamline PXII with a Pilatus 6M detector (Dectris) or PXIII with a Pilatus 2M (Dectris) or MarCCD 225 detector (Mar

581 Research). Data were processed with *XDS*[48], scaled further with *AIMLESS*[49] using
582 *aP_SCALE*[50], and converted to structure factor amplitudes with *TRUNCATE* supported by other
583 programs in the CCP4 suite[51].

584 Two related hexagonal crystal forms that diffracted to 4 Å resolution were obtained from the
585 same conditions: from A with unit cell dimensions $a = b$ = ~203 Å, c = ~197 Å, and form B with
586 unit cell dimensions $a = b$ = ~208 Å, c = ~167 Å. The C-terminal region of the Rif1-NTD (Rif1-
587 NTD SHAFT) in crystal form B was disordered and these crystals were only used for early phase
588 improvement by cross-crystal averaging.

589 Diffraction data sets to a maximum resolution (d_{min}) of 5.35 Å resolution were obtained from a
590 SeMet-substituted Rif1-NTD (residues 177-1283) crystal (data set SeMet-1) at the absorption
591 peak and inflection point of the selenium K-edge. In a MAD phasing approach, heavy atom sites
592 located by *SHELXD*[52] using the anomalous differences between 15-6.7 Å resolution were
593 refined with *autoSHARP*[53]. From a substructure of 20 atoms, this gave an electron density map
594 at 5.35 Å resolution and established the space group as $P6_522$ with a single Rif1-NTD copy in
595 the asymmetric unit with ~70% solvent. The α-helical disposition of the Rif1-NTD was readily
596 identified from the arrays of tubular electron density in the initial map. Side chain features were,
597 however, absent. Starting with the initial electron density map and the SeMet-1 absorption peak
598 data, the anomalous substructure was re-determined using MR-SAD with *PHASER*[54], which
599 located the 23 unique selenium positions in the crystal. A model was built from ideal poly-
600 alanine α-helices into the initial electron map with *COOT*[55], relating the spacing of the selenium
601 sites to the methionine positions in the Rif1-NTD amino acid sequence to infer its directionality.
602 The MR-SAD phases were improved by cross-crystal averaging with a form B crystal (d_{min} = 4.0
603 Å) using *DMMULTI*[56], which produced an electron density map showing some side chain
604 protrusions. The α-helical model was extended into this map and the amino acid sequence was
605 assigned in regions supported by electron density using the selenium substructure as

606 methionine markers. Further details of phasing, model building and refinement procedures are
607 in the Supplementary note.

608 The final model contains all residues from 185 to 1273 except residues 685-693 of insertion
609 Loop-II (LOOP) and residues 1245-1275 of the final loop, which were unmodeled because of
610 disorder. Owing to conformational flexibility, the quality of the electron density for the C-terminal
611 SHAFT domain was considerably poorer than other regions of the Rif1-NTD. Data collection
612 and refinement statistics are in Table 1.

613 **Rif1-NTD–DNA structure determination**

614 Rif1-NTD (residues 100-1322) formed crystals with 30 bp dsDNAs bearing a 24 or 30 nt 3′-tail
615 (oligonucleotides 15+2 or 1+2 in Supplementary Table 1). The crystals were grown from a
616 mixture of 43.5 μM protein and 65 μM DNA in storage buffer by dehydrating a 1 μL of Rif1-NTD–
617 DNA solution by sitting drop vapor diffusion over a reservoir containing 10 mM $NiCl_2$, 100 mM
618 Tris-HCl, pH 8, 20% (w/v) polyethylene glycol MME 2000. Crystals appeared within 3 d and
619 were harvested after 1 week. For cryo-protection, the crystal-growth drop was covered with a
620 thin layer of 25% (v/v) PEG 400 made up in storage buffer after which a single crystal was
621 quickly removed and flash-cooled in liquid nitrogen.

622 Diffraction data were collected and processed as described for the Rif1-NTD in isolation except
623 the averaged intensities were corrected for anisotropy and converted to structure factor
624 amplitudes with *STARANISO* (v. 1.0.4, Global Phasing Ltd.), applying a 1 $I/\sigma I$ anisotropic high-
625 resolution cut-off.

626 The Rif1-NTD–DNA crystals were similar: all belonged to space group $P2_12_12_1$ and had
627 approximate unit cell parameters a = 87 Å, b = 164 Å, c = 387 Å. Diffraction was weak and
628 strongly anisotropic. Two crystals were characterized: Rif1-NTD–DNA-I containing 30 bp dsDNA
629 with a 24 nt 3′-tail that diffracted to 5.2 Å resolution; and Rif1-NTD–DNA-II containing 30 bp

dsDNA with a 30 nt 3′-tail that diffracted to 7.5 Å resolution (assuming an isotropic high-resolution $CC_{1/2}$ cut-off of 0.3 in both cases). Details of molecular replacement, DNA identification, model building, and refinement procedures are in the Supplementary note. Full details of the data collection and refinement statistics, including anisotropy analysis for Rif1-NTD–DNA-II are in Table 1.

Surface electrostatic potentials were calculated with APBS[57]. Structural figures were prepared with PyMOL (v. 1.8.2, Schrödinger).

DNA substrates for electromobility shift assays (EMSA)

Polyacrylamide gel electrophoresis (PAGE)-purified DNA oligonucleotides were obtained from Microsynth (Switzerland) (Supplementary Table 1). DNA concentration was measured by UV absorption using a Nanodrop spectrophotometer (Thermo Scientific). For EMSA, oligonucleotides were labeled by T4 polynucleotide kinase (New England Biolabs) and (γ-^{32}P)ATP at 37°C for 1 h. Reactions were stopped by adding 20 mM EDTA. Oligonucleotides were desalted into 10 mM Tris-HCl pH 8.0, 1 mM $MgCl_2$ and 50 mM NaCl using an Illustra MicroSpin G-25 column (GE healthcare). DNA oligonucleotides at 2 µM were mixed in the combinations listed in Supplementary Table 2 and annealed in 10 mM Tris-HCl pH 8, 1 mM $MgCl_2$, 50 mM NaCl by heating for 5 min to 98°C and cooling at 1°C/min to 4°C. Annealed DNA substrates (20 µL) were purified by 14% PAGE electrophoresis at 4°C and stored in 10 mM Tris-HCl pH 8.0, 1 mM EDTA at 4°C.

Electromobility shift assays (EMSAs) and quantification

Protein concentrations were measured by the Bradford method with a bovine serum albumin (BSA) standard and UV absorption Nanodrop spectrophotometer (Thermo Scientific). EMSAs were performed in a buffer containing 20 mM Tris-HCl pH 8.0, 100 mM NaCl, 2.5 mM $MgCl_2$, 10 mM $CaCl_2$, 0.1 mg/mL BSA, 1 mM TCEP. For simple EMSA titrations (Fig. 2a, e and

Supplementary Fig. 2i), the labelled DNA at a final concentration of 1 nM was added to the serially diluted protein to obtain the concentrations indicated. The mixture was incubated for 20 min at 20°C prior to analysis. For equimolar titrations (Supplementary Fig. 2j, l), labelled DNA (1 nM final concentration) was added to the protein to obtain the final concentrations indicated. Serially diluted unlabeled DNA was then added to the mixture at the indicated concentrations. The mixture was incubated for 20 min at 20°C prior to analysis.

Preincubated protein-DNA solutions were mixed with glycerol at a final concentration of 8% (v/v) and 10 µL sample was separated by 1.2% (w/v) agarose gel electrophoresis in 0.5 × TBE at 4°C for 2 h at 150 V. The gels were dried on DE81 chromatography paper (Whatman), exposed to storage phosphor screens (GE Healthcare), scanned by a Typhoon phosphor imager (GE Healthcare).

EMSA images were quantified with ImageJ[58]. Bands were defined across the gel and noise was subtracted. The intensity of the analyzed bands was normalized to the total intensity of the lane. The percentages of intensities were plotted (Fig. 2b, 2e and Supplementary Fig. 2k) using GraphPad Prism 6. The K_d was calculated assuming specific binding with a Hill slope ($Y = Bmax*X^h/(Kd^h + X^h)$) (Fig. 2b). The mean and standard error of the mean were calculated with GraphPad Prism (Fig. 2e and Supplementary Fig, 2k).

Negative stain EM

For negative stain EM without DNA, Rif1-NTD (residues 100-1322) was re-purified by size exclusion chromatography (Superdex 200, GE Healthcare). For EM with DNA, oligonucleotide no. 2 and 4 (Supplementary Table 1) were equilibrated against 50 mM HEPES pH 7.4, 150 mM NaCl, 10 mM $MgCl_2$, 1 mM TCEP and annealed in this buffer by heating for 5 min to 98°C and cooled at 1°C/min to 4°C, forming a 30 bp dsDNA bearing a 30 nt 3′-tail. A sample of suitable homogeneity for EM analysis was obtained by mixing Rif1-NTD with a threefold molar excess of

678 3′-tailed DNA. For EM sample preparation, 20 µM of Rif1-NTD was mixed with 60 µM of
679 annealed DNA and was incubated for 15 min on ice prior to separation in a glycerol gradient
680 (10-20% w/v) by ultracentrifugation for 16 h at 214000*g* (4°C). Fractions containing Rif1-NTD
681 with or without DNA were diluted to ~0.1 mg/mL and absorbed to glow-discharged Quantifoil
682 grids coated with a continuous thin carbon film (S7/2, Cu 400 mesh, 2 nm carbon film, Quantifoil
683 Micro Tools). A 4 µL sample was applied to a grid and negatively stained with 2% (w/v) uranyl
684 acetate. Data were acquired using a Philips CM200FEG transmission electron microscope
685 operated at 200 kV. Images were recorded in low-dose mode with a TVIPS F416 camera (Tietz
686 Video and Image Processing Systems) at a nominal magnification of 50,000×, resulting in a
687 pixel size of 2.2 Å at the sample. A defocus range -0.5 µm to -5 µm was used for data
688 acquisition.

689 For Rif1-NTD in isolation, 10091 particles were manually selected from 100 micrographs using
690 *e2boxer.py* from EMAN2[59] and extracted with a box size of 150 × 150 pixels. For the sample
691 with DNA 39981 particles were selected from 500 micrographs and extracted with a box size of
692 180 × 180 pixels. A detailed description of the negative stain analysis using SPARX[60] and
693 RELION[61] can be found in the Supplementary note.

694 The models shown in Supplementary Fig. 2d and 2e were auto-refined by RELION[61] to a
695 maximum resolution of 36 Å Rif1-NTD in isolation and 33 Å for Rif1-NTD+DNA. DNA was not
696 visible, as expected given the resolution and the negative stain conditions.

697 **Yeast techniques**

698 Genotypes of all *Saccharomyces cerevisiae* strains are given in Supplementary Table 3. All
699 strains are long-term stored at -80°C using glycerol-based storage medium. General yeast
700 manipulations were done according to standard methods[62]. Deletions and epitope tagging of
701 genes of interest were done by one-step PCR gene replacement[63]. Point mutations and

deletions in the *RIF1* gene were introduced using the delitto perfetto method[64]. Rapid depletion of endogenous Rif1 was achieved using the anchor-away method to sequester Rif1 by cytoplasmic anchoring[34]. For drop assays, strains were grown exponentially (OD_{600} ~0.4) and serial 10-fold dilutions were then spotted on agar plates containing YPAD or selective medium. Plates were recorded after 2-3 d incubation at the indicated temperatures.

Single-cell checkpoint arrest analysis (G2/M assay)

The G2/M cell-cycle arrest assay was performed as described[15] with minor modifications. Cells containing a unique HO endonuclease site flanked by TG80 arrays were grown for 12-14 h in YPAD, then diluted to OD_{600} = 0.1 in YPLG (2% lactic acid, 3% glycerol) and grown for 3 h before HO endonuclease induction by addition of 2% (w/v) galactose. After 2 h, single small-budded cells were dissected on a grid on YPAD plates and analyzed. Every 30 min, cells were checked for cell-cycle restart as indicated by a second round of budding.

Western blotting

Western blots were performed as described[2] using the following antibodies: Anti-Myc (Cell Signaling, mAb #2276) and Anti-Actin (Abcam, Ab 8224).

Chromatin immunoprecipitation (ChIP)

To detect enrichment of proteins in proximity of HO endonuclease cut sites, cell cultures were grown in YPLG medium for 3 h and the HO endonuclease was then induced by adding 2% (w/v) galactose. ChIP was then performed as reported previously[15]. For ChIP analyses at native telomeres, exponentially growing cells in YPAD at the indicated temperatures were collected and ChIP was performed as described[2]. The following antibodies were used for ChIP analysis: Anti-Myc (9E10 from culture supernatant), Anti-Rap1 (culture supernatant) and Anti-RPA (Pierce Biotechnology, scRPA PA1-10301). Primer sequences are available upon request.

Quantification of ssDNA as a measure of 5′-3′ DNA end-resection

Genomic DNA was extracted by a phenol/chloroform and 2-propanol method from 25-50 mL of cell cultures and digested overnight with *Alu*I[44]. qPCR was performed using GoTaq qPCR Master Mix (Promega). To detect the formation of ssDNA, primer pairs (sequences available upon request) flanking *Alu*I in the proximity of an HO endonuclease-induced DSB were used. *Alu*I sites that have been converted to ssDNA by end-resection are resistant to cleavage, leading to increased qPCR product yield. To normalize the data, qPCR amplifications of genomic regions devoid of *Alu*I sites (located at the promoter region of the *HMO1* gene or in the *SMC2* locus) were performed. qPCR reactions were carried out to assess the efficiency of DSB induction by the HO endonuclease as described[65] Calculation of % ssDNA was performed for each time point as described[44].

NHEJ assays

The efficiency of NHEJ as measured by cell survival was determined as described[35,36]. JKM179-derived strains (see Supplementary Table 3) were grown overnight in YPAD, then diluted in YPLG and grown exponentially. For transient HO endonuclease expression, 2% (w/v) galactose was added to the culture medium. At the indicated time points, cells were plated on glucose-containing YPAD agar plates. For reference, cells were removed prior to HO endonuclease induction and plated on glucose-containing medium. HO endonuclease cut efficiency was routinely determined by qPCR[65] and data were normalized accordingly. Colonies were counted 3 d after plating. NHEJ efficiency was calculated as described[35]. For chronic HO endonuclease expression, cells were plated on medium containing 2% (w/v) galactose and, in parallel, on medium containing glucose. Colonies were counted 3-4 d after plating, and the efficiency of imprecise NHEJ efficiency was calculated as described[35].

Cell viability in the presence of Zeocin

749 Exponentially growing cells were plated on YPAD agar containing Zeocin (Zeocin Selection
750 Reagent, ThermoFisher Scientific) and on drug-free plates to determine the plating efficiency by
751 colony outgrowth after incubation for 3-4 d. Resistance of mutant strains to 70 µg/mL Zeocin
752 (Fig. 4d and Supplementary Fig. 5e) was determined relative to wild-type cells. Cell survival on
753 exposure to increasing Zeocin concentrations (Supplementary Fig. 5f) was measured by colony
754 outgrowth against cells of the same strain grown on drug-free plates.

755 **Southern blotting**

756 For the analysis of telomere length, genomic DNA was digested with *Xho*I, separated on a 0.8%
757 (w/v) agarose gel and transferred to nylon membrane. Transferred DNA was probed with a
758 ^{32}P-radiolabelled TG-repeat probe and detected by autoradiography. Analysis of DNA end-loss
759 was performed as described[42]. Genomic DNA was digested with *EcoR*V, separated on 0.8%
760 (w/v) agarose gels, and transferred overnight to nylon membranes. Transferred DNA was
761 crosslinked to the membrane by baking (80°C, 1 h), and probed with ^{32}P-radiolabeled DNA
762 fragments mapping near the HO cut site at the *MATα* locus on chromosome III and the *SMC2*
763 locus on chromosome VI. The amount of DNA in each band was determined using a
764 PhosphorImager with Fiji software. The percentage of remaining DNA ends was calculated as
765 described previously[42].

766 **Statistical analysis**

767 Quantification of average restart times (t) in single-cell checkpoint arrest assays (Figure 3c) and
768 determination of P-values was done using a Kaplan-Meier survival analysis. A log rank test was
769 used to compare the curves with each other using the Holm-Sidak method for pairwise
770 comparisons as described previously[15]. Statistical analysis of the anchor-away assay results
771 (Fig. Supplementary Fig. 4 d – g) was performed using an unequal variance t-test (Welch test)
772 in GraphPad Prism 7, comparing cultures with and without depletion of Rif1. Statistical analysis

of NHEJ efficiency (Supplementary Fig. 5a) was performed using a one-way ANOVA test followed by a post-hoc Tukey-Kramer multiple comparison test. P-values and degrees of freedom are reported in the figure and figure legend.

Data availability

Atomic coordinates and structure factors have been deposited in the PDB under accession codes 5NVR and 5NW5. Uncropped images of EMSAs, Western and Southern blots are in the Supplementary Data Set. All reagents, protocols and other data in this study are available from the authors upon request.

Methods-only References

47. Cronin, C.N., Lim, K.B. & Rogers, J. Production of selenomethionyl-derivatized proteins in baculovirus-infected insect cells. *Protein Sci.* **16**, 2023-2029 (2007).

48. Kabsch, W. XDS. *Acta Cryst. D* **66**, 125-132 (2010).

49. Evans, P.R. & Murshudov, G.N. How good are my data and what is the resolution? *Acta Cryst. D* **69**, 1204-1214 (2013).

50. Vonrhein, C. et al. Data processing and analysis with the autoPROC toolbox. *Acta Cryst. D* **67**, 293-302 (2011).

51. Winn, M.D. et al. Overview of the CCP4 suite and current developments. *Acta Cryst. D* **67**, 235-242 (2011).

52. Sheldrick, G. A short history of SHELX. *Acta Cryst. A* **64**, 112-122 (2008).

53. Vonrhein, C., Blanc, E., Roversi, P. & Bricogne, G. Automated Structure Solution With autoSHARP. in *Macromolecular Crystallography Protocols: Volume 2: Structure Determination* (ed. Doublié, S.) 215-230 (Humana Press, Totowa, NJ, 2007).

54. McCoy, A.J. et al. Phaser crystallographic software. *J. Appl. Cryst.* **40**, 658-674 (2007).

55. Emsley, P., Lohkamp, B., Scott, W.G. & Cowtan, K. Features and development of Coot. *Acta Cryst. D* **66**, 486-501 (2010).

56. Cowtan, K. 'dm': An automated procedure for phase improvement by density modification. *Joint CCP4 and ESF-EACBM Newsletter on Protein Crystallography* **31**, 34-38 (1994).

57. Baker, N.A., Sept, D., Joseph, S., Holst, M.J. & McCammon, J.A. Electrostatics of nanosystems: Application to microtubules and the ribosome. *Proc. Natl. Acad.Sci.***98**, 10037-10041 (2001).

58. Schneider, C.A., Rasband, W.S. & Eliceiri, K.W. NIH Image to ImageJ: 25 years of image analysis. *Nat. Meth.* **9**, 671-675 (2012).

59. Tang, G. et al. EMAN2: An extensible image processing suite for electron microscopy. *J. Struct. Biol.* **157**, 38-46 (2007).

60. Hohn, M. et al. SPARX, a new environment for Cryo-EM image processing. *J. Struct. Biol.* **157**, 47-55 (2007).

61. Scheres, S.H. RELION: implementation of a Bayesian approach to cryo-EM structure determination. *J. Struct. Biol.* **180**, 519-30 (2012).

62. Rose, M.D., Winston, F., and Hieter P. Methods in yeast genetics: a laboratory course manual. *Plainview, New York: Cold Spring Harbor Press* (1990).

63. Longtine, M.S. et al. Additional modules for versatile and economical PCR-based gene deletion and modification in Saccharomyces cerevisiae. *Yeast* **14**, 953-61 (1998).

64. Stuckey, S., Mukherjee, K. & Storici, F. In vivo site-specific mutagenesis and gene collage using the delitto perfetto system in yeast Saccharomyces cerevisiae. *Methods Mol. Biol.* **745**, 173-91 (2011).

65. Horigome, C. et al. SWR1 and INO80 chromatin remodelers contribute to DNA double-strand break perinuclear anchorage site choice. *Mol. Cell* **55**, 626-39 (2014).

Figure 1

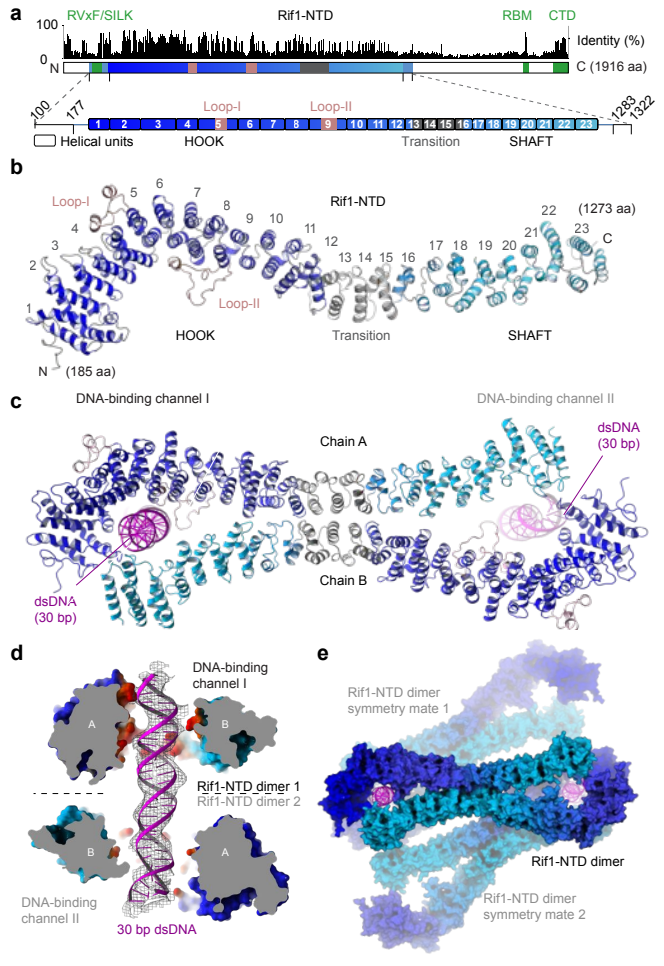
a
RVxF/SILK
Rif1-NTD
RBM
CTD
100
0
N
Identity (%)
C (1916 aa)
100
177
Loop-I
Loop-II
1283
1322
1 2 3 4 5 6 7 8 9 10 11 12 13 14 15 16 17 18 19 20 21 22 23
Helical units
HOOK
Transition
SHAFT
b
Loop-I
Rif1-NTD
(1273 aa)
Loop-II
HOOK
Transition
SHAFT
N
(185 aa)
C
c
DNA-binding channel I
DNA-binding channel II
Chain A
Chain B
dsDNA
(30 bp)
dsDNA
(30 bp)
d
DNA-binding
channel I
A
B
Rif1-NTD dimer 1
Rif1-NTD dimer 2
B
A
DNA-binding
channel II
30 bp dsDNA
e
Rif1-NTD dimer
symmetry mate 1
Rif1-NTD dimer
Rif1-NTD dimer
symmetry mate 2

Figure 2

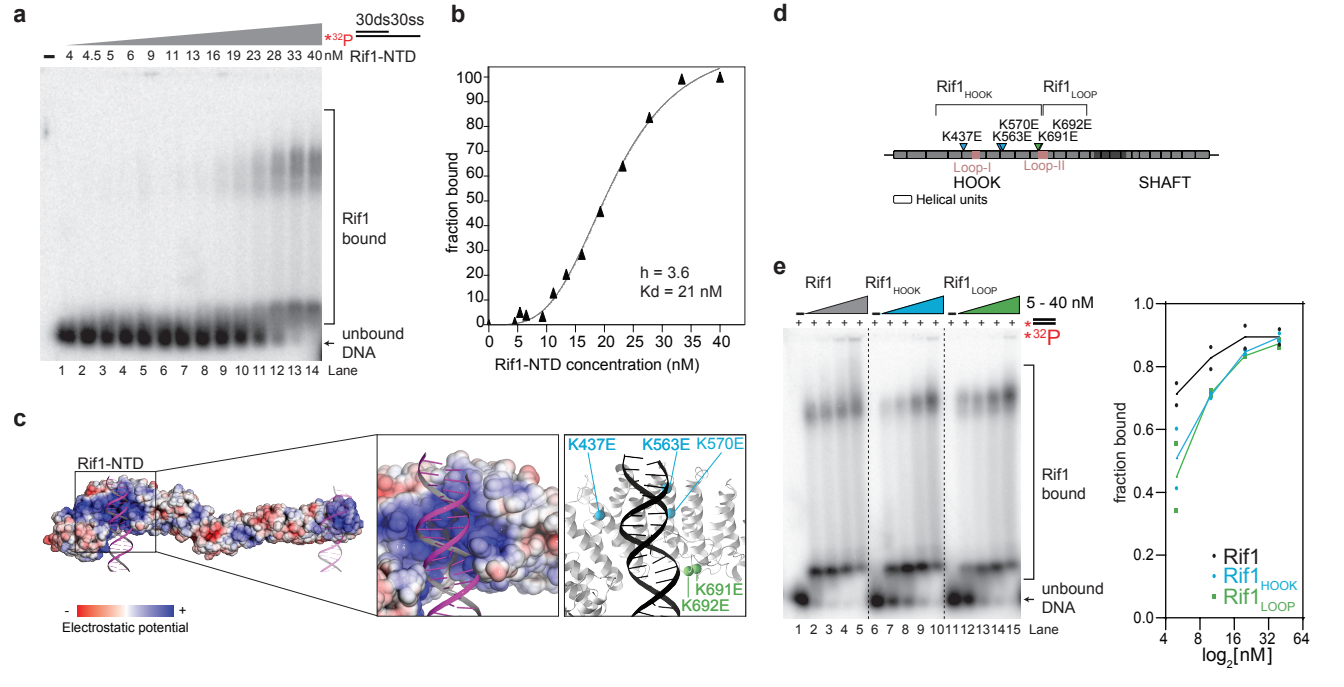
a
30ds30ss
*32P
– 4 4.5 5 6 9 11 13 16 19 23 28 33 40 nM Rif1-NTD
Rif1 bound
unbound DNA
1 2 3 4 5 6 7 8 9 10 11 12 13 14 Lane
b
fraction bound
h = 3.6
Kd = 21 nM
Rif1-NTD concentration (nM)
c
Rif1-NTD
K437E
K563E
K570E
K691E
K692E
Electrostatic potential
d
Rif1HOOK
Rif1LOOP
K570E
K692E
K437E
K563E
K691E
Loop-I
Loop-II
HOOK
SHAFT
Helical units
e
Rif1
Rif1HOOK
Rif1LOOP
5 - 40 nM
*32P
Rif1 bound
unbound DNA
1 2 3 4 5 6 7 8 9 10 11 12 13 14 15 Lane
fraction bound
Rif1
Rif1HOOK
Rif1LOOP
log2[nM]

Figure 3

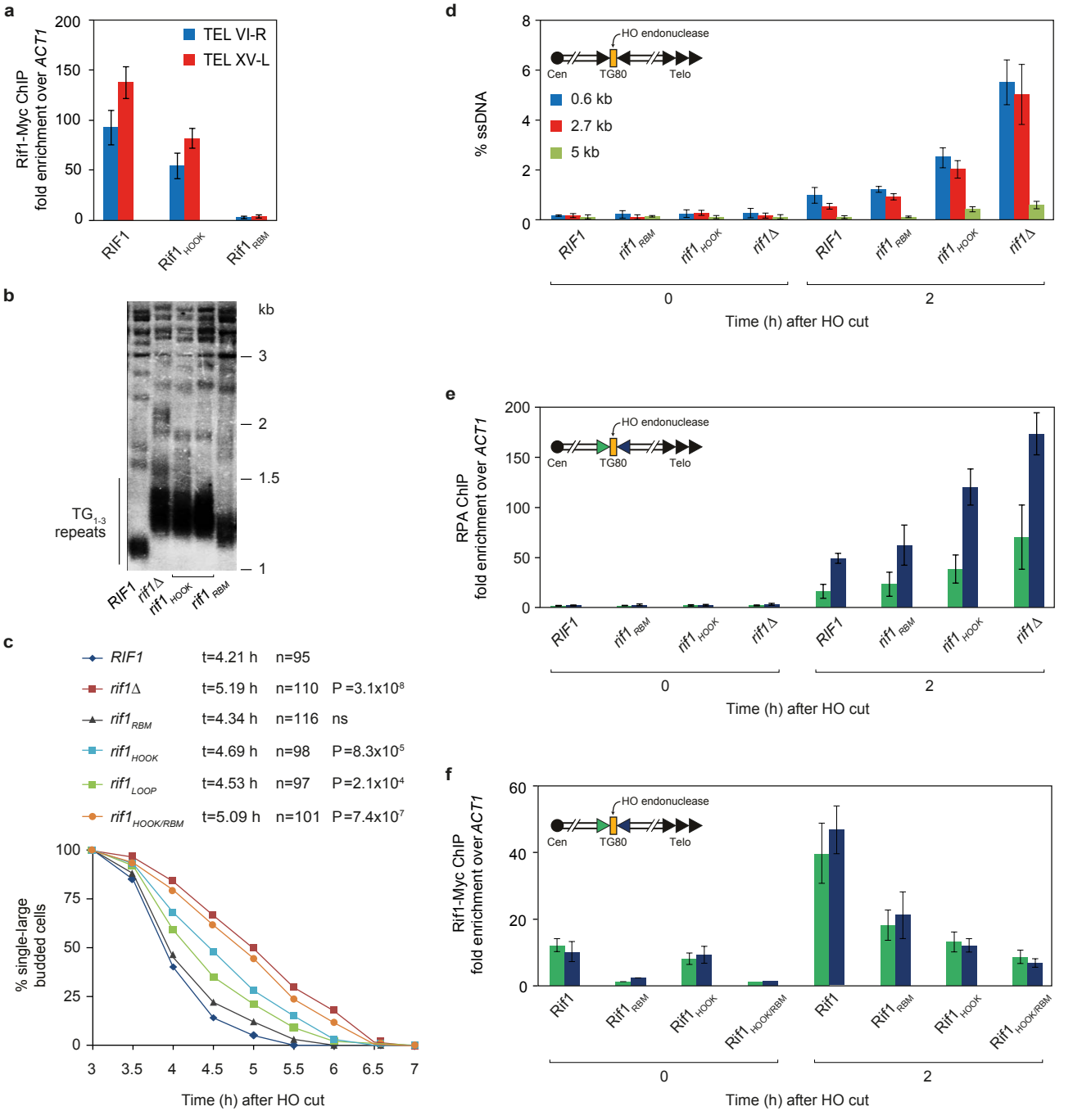
a
Rif1-Myc ChIP
fold enrichment over ACT1
TEL VI-R
TEL XV-L
RIF1
Rif1 HOOK
Rif1 RBM
b
kb
TG1-3
repeats
RIF1
rif1Δ
rif1 HOOK
rif1 RBM
c
RIF1 t=4.21 h n=95
rif1Δ t=5.19 h n=110 P =3.1x10^8
rif1 RBM t=4.34 h n=116 ns
rif1 HOOK t=4.69 h n=98 P=8.3x10^5
rif1 LOOP t=4.53 h n=97 P=2.1x10^4
rif1 HOOK/RBM t=5.09 h n=101 P=7.4x10^7
% single-large budded cells
Time (h) after HO cut
d
% ssDNA
HO endonuclease
Cen
TG80
Telo
0.6 kb
2.7 kb
5 kb
Time (h) after HO cut
e
RPA ChIP
fold enrichment over ACT1
f
Rif1-Myc ChIP
fold enrichment over ACT1

Figure 4

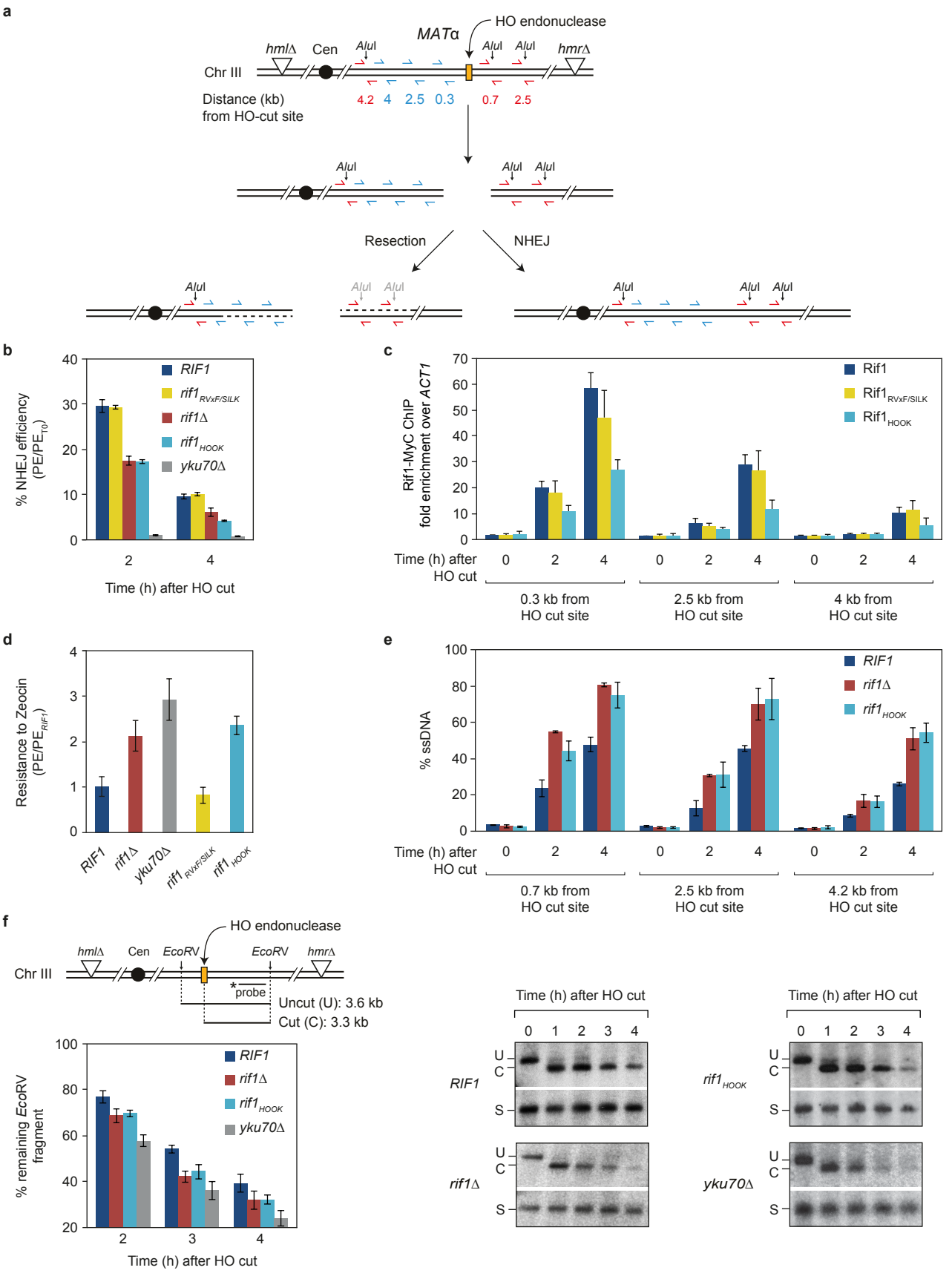
a
MATα
HO endonuclease
hmlΔ
Cen
AluI
hmrΔ
Chr III
Distance (kb)
from HO-cut site
4.2 4 2.5 0.3 0.7 2.5
Resection
NHEJ
b
% NHEJ efficiency
(PE/PE$_{T0}$)
RIF1
rif1$_{RVxF/SILK}$
rif1Δ
rif1$_{HOOK}$
yku70Δ
Time (h) after HO cut
c
Rif1-MyC ChIP
fold enrichment over ACT1
Rif1
Rif1$_{RVxF/SILK}$
Rif1$_{HOOK}$
Time (h) after HO cut
0.3 kb from HO cut site
2.5 kb from HO cut site
4 kb from HO cut site
d
Resistance to Zeocin
(PE/PE$_{RIF1}$)
RIF1
rif1Δ
yku70Δ
rif1$_{RVxF/SILK}$
rif1$_{HOOK}$
e
% ssDNA
RIF1
rif1Δ
rif1$_{HOOK}$
Time (h) after HO cut
0.7 kb from HO cut site
2.5 kb from HO cut site
4.2 kb from HO cut site
f
HO endonuclease
EcoRV
probe
Uncut (U): 3.6 kb
Cut (C): 3.3 kb
% remaining EcoRV fragment
RIF1
rif1Δ
rif1$_{HOOK}$
yku70Δ
Time (h) after HO cut
U
C
S

Figure 5

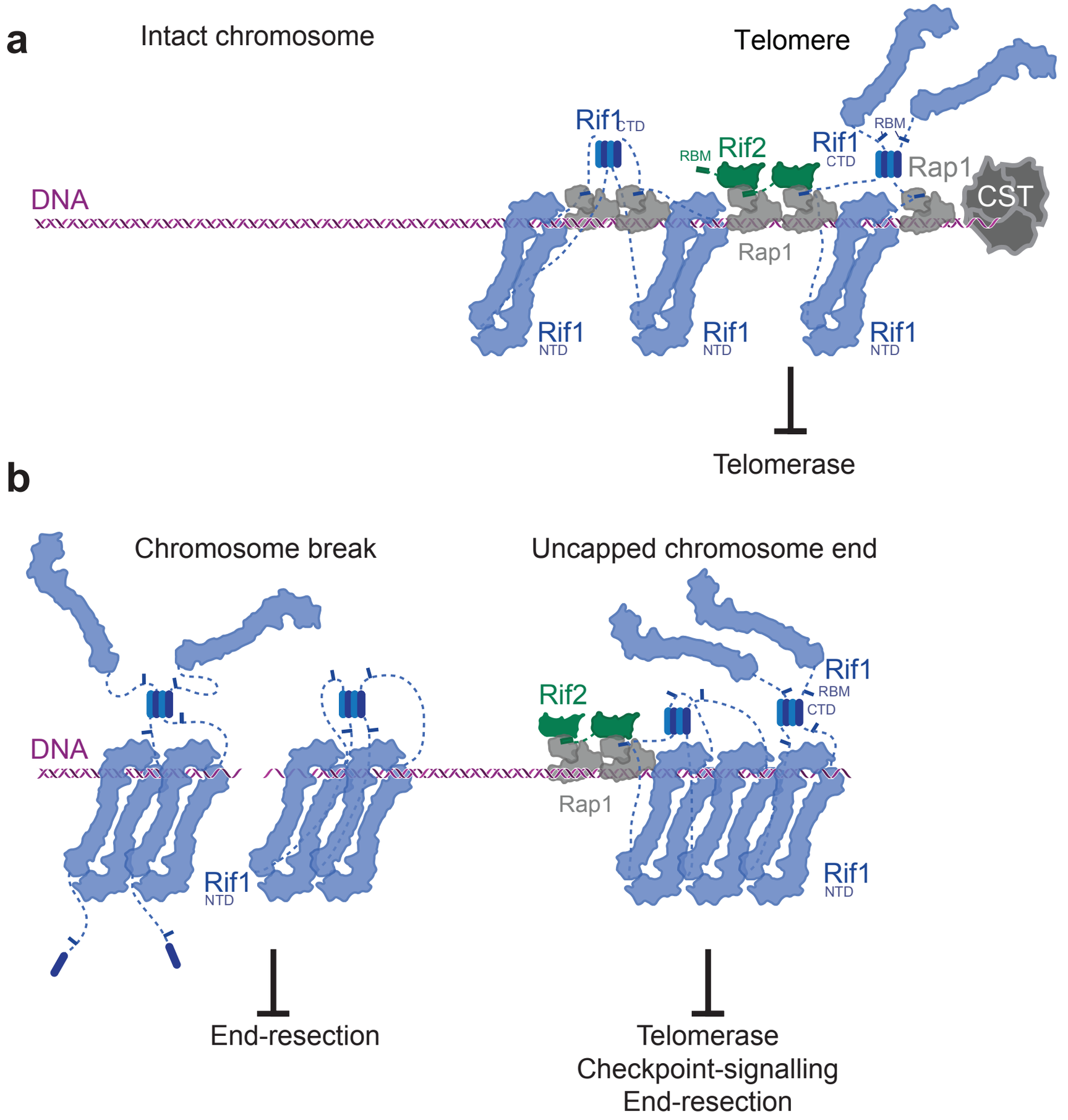
a
Intact chromosome
Telomere
Rif1 CTD
RBM
Rif2
Rif1 CTD
RBM
Rap1
CST
DNA
Rap1
Rif1 NTD
Rif1 NTD
Rif1 NTD
Telomerase
b
Chromosome break
Uncapped chromosome end
Rif1
RBM
CTD
Rif2
DNA
Rap1
Rif1 NTD
Rif1 NTD
End-resection
Telomerase
Checkpoint-signalling
End-resection